In Situ Observations of Early Stage Oxidation of Ni-Cr and Ni-Cr-Mo Alloys

Xiao-xiang Yu,[‡,] Ahmet Gulec,[*] Christopher M. Andolina,[**] Evan J. Zeitchick,[***] Kateryna Gusieva,[****] Judith C. Yang,[**] John R. Scully,[****] John H. Perepezko,[***] and Laurence D. Marks[*]*

ABSTRACT

Results of in situ transmission electron microscopy experiments on the early stage oxidation of Ni-Cr and Ni-Cr-Mo alloys are reported. An epitaxial rock-salt oxide with compositions outside the conventional solubility limits initiated at the surface of both alloys, progressing by a layer-by-layer mode. Kirkendall voids were found in Ni-Cr alloys near the metal/oxide interface, but were not seen in the Ni-Cr-Mo. The voids initiated in the oxide then diffused to the metal/oxide interface, driven by the misfit stresses in the oxide. A sequential oxide initiation was observed in NiCr alloys: rock-salt → spinel → corundum; however, for NiCrMo alloys, the metastable $Ni_{2-x}Cr_xO_3$ (corundum structure) phase formed shortly after the growth of the rock-salt phase. Chemical analysis shows that solute atoms were captured in the initial oxide before diffusing and transforming to more thermodynamically stable phases. The results indicate that Mo doping inhibits the formation of Kirkendall voids via an increase in the nucleation rate of corundum, which was verified by density functional theory calculations.

KEY WORDS: density functional theory (DFT), in situ environmental transmission electron microscope (ETEM), Kirkendall voids, molybdenum, nickel-based alloys, oxidation

INTRODUCTION

Nickel-based superalloys are widely used structural materials because of their excellent combination of strength, ductility, and corrosion resistance at elevated temperature.[1] Comprehensive experimental and theoretical investigations show that the general oxidation behavior depends on the composition and exposure conditions such as temperature and pressure of oxygen.[2] The continuous oxide scale, which protects the underlying metal surface, usually contains single or multiple phases which are typically interpreted as stoichiometric oxides, such as rock-salt NiO, corundum Cr_2O_3 and Al_2O_3, and spinel $NiCr_2O_4$, with some solute atoms within thermodynamic solubility limits.[3] Although extensive studies[4-6] have been conducted on the thermodynamically stable oxide scales formed after hours or days, the early stages from oxide initiation to the formation of a several nanometers thick film on the alloy surface are not well understood. A retroactive analysis of oxidized samples does not provide a complete picture of oxide nucleation, growth, and coarsening. In contrast, in situ environmental transmission electron microscopy (ETEM) can provide a unique way to monitor the development process. Although a few in situ studies have been performed on the oxidation of Ni-Cr and

Submitted for publication: March 2, 2018. Revised and accepted: June 1, 2018. Preprint available online: June 1, 2018, https://doi.org/10.5006/2807.
‡ Corresponding author. E-mail: yuxx07@gmail.com.
* Department of Materials Science and Engineering, Northwestern University, Evanston, IL.
** Department of Chemical and Petroleum Engineering, University of Pittsburgh, Pittsburgh, PA.
*** Department of Materials Science and Engineering, University of Wisconsin-Madison, Madison, WI.
**** Department of Materials Science and Engineering, The University of Virginia, Charlottesville, VA.

ISSN 0010-9312 (print), 1938-159X (online)

Ni-Al alloys,[7-11] the subsequent phase transition and oxide evolution at the atomic scale are relatively unknown.[12]

Beyond the base alloys, the addition of minor alloying elements such as molybdenum (Mo) to the nickel-based alloys can have positive or negative impacts on the oxidation and corrosion behavior depending on the environment.[13] For high-temperature oxidation in dry air, Mo may have favorable effects on the selective oxidation of chromium,[14] but the formation of volatile MoO_3 degrades the oxidation resistance.[15] In different environments, Mo has been found to enhance the hot corrosion resistance in a chloride-containing vapor,[16-17] as well as improve the passivation, pitting resistance, and crevice corrosion in aqueous chloride media.[18-25] However, the details of how and why Mo changes the oxidation are still unclear and the synergetic mechanism of Mo and Cr in aqueous corrosion resistance is under active debate.

In this paper, the results of in situ TEM experiments on the early stage oxidation of Ni-Cr and Ni-Cr-Mo alloys are reported in dry oxygen gas at elevated temperature. An initial epitaxial growth of rock-salt oxides on the surfaces of both alloys was observed, growing by the layer-by-layer mode. A sequence of oxide initiation and phase separation has been observed in NiCr alloys: rock-salt → spinel→ corundum, with compositions beyond the thermodynamic stability limits. Kirkendall voids[26-30] nucleate in the oxide and diffuse to the metal/oxide interface, driven by the misfit stresses. In contrast, for NiCrMo alloys the metastable $Ni_{2-x}Cr_xO_3$ (corundum structure) phase formed shortly after the growth of epitaxial rock-salt, and no Kirkendall voids formed. The metastable phase is a consequence of non-equilibrium solute capture during formation of the oxide as discussed elsewhere in more detail.[31] The experimental evidence indicates that Mo stabilizes individual cation vacancies by promoting the formation of a corundum phase, which is analyzed in terms of valence accommodation by the Mo and with specific density functional theory (DFT) calculations.

EXPERIMENTAL AND COMPUTATIONAL DETAILS

Ni-22%Cr and Ni-22%Cr-6%Mo (wt%) sample bars were prepared in an arc furnace and the alloys were homogenized in a tube furnace at 1,000°C for 5 h followed by a water quench. The heat treatment eliminates the solidification microstructure and chemical segregation, forming uniformly sized grains (on a micrometer scale). TEM samples were prepared using a low-speed saw (Buehler, Isomet[†]) to cut the bulk sample into thin slices (~0.7 mm), then mechanically thinned to less than 100 μm using sandpapers. Several 3 mm diameter disks were cut with a disk cutter (South Bay Technology, Model 360[†]) and dimpled (VCR group, Inc., D500i[†]) using a diamond suspension to a final thickness <10 μm. Once dimpled, the discs were argon ion milled at 3 keV ~ 6 keV (Gatan precision ion polishing system, Model 691[†]) until a small hole in the sample center appeared.

The in situ oxidation experiments were performed in a dedicated LaB_6 environmental TEM (Hitachi H9500[†]) operated at 300 kV at the University of Pittsburgh. The microscope is equipped with a double tilt heating holder (Hitachi High Technologies, Inc.) and a homebuilt gas injection system. The samples were first reduced in hydrogen gas (99.5% Matheson Tri-Gas[†]) at 1.1×10^{-2} Pa and 700°C to remove native oxides and other contaminants such as adventitious carbon, which was confirmed by selected area electron diffraction. The flow of the reducing atmosphere was then stopped at the AliCat[†] mass flow controller (AliCat Scientific) and the injection gas lines and the ETEM column were pumped to the base pressure (6.0×10^{-6} Pa). The AliCat controlling the O_2 (Matheson, 99.5%) gas was then set to a suitable value of ~0.700 sccm while the gas delivery system was opened to the roughing pump vacuum. After the flow had stabilized (10 s) at the selected sccm, the gas delivery valve was opened on the ETEM and the valve to the gas handling system vacuum was closed. The oxygen column pressure stabilized after 15 s at 1.3×10^{-2} Pa and 700°C. High definition videos were collected during the oxidation process at 3 frames/s with an exposure time of 0.333 s.

Analysis on the postmortem samples after the in situ experiments was performed by scanning transmission electron microscope (STEM), an aberration-corrected JEOL JEM-ARM200CF[†] at the University of Illinois at Chicago with collections angles 90 mrad ≤ β ≤ 220 mrad for high angle annular dark field imaging. Compositional analysis was performed with a Gatan Enfina[†] electron energy loss spectroscopy (EELS) attached to the microscope.

To elucidate the role of Mo on the Kirkendall void suppression and corundum structure formation, spin-polarized DFT calculations were performed using the Vienna Ab initio Simulation Package[†] (VASP)[32-34] with the projector augmented wave method.[35] The exchange-correlation energy was evaluated using the meta-generalized gradient approximation (meta-GGA) MS2[36-37] in all of the simulations, leading to reasonable values for the lattice parameters, band gap, formation energies, and magnetic moment. Note that because the interest later will only be in formation energies, there is no reason to add exchange corrections to improve the band gap. A 550 eV was chosen for the plane wave cutoff and the k points sampling used the Monkhorst–Pack scheme.[38] The electronic structures were relaxed with a convergence of 10^{-5} eV for the total energy and the atomic structures were

[†] Trade name.

relaxed until the forces on each ion were less than 0.01 eV/Å.

RESULTS

Initial Growth of Rock-Salt Structure

Immediately after the introduction of oxygen gas, a rock-salt structure similar to NiO initiated at the surface of both Ni-Cr and Ni-Cr-Mo, as shown in Figures 1(a) and (b). It is important to clarify that only the structure is similar to NiO, not that it is NiO, because the composition is not that of the simple stoichiometric compound; an alternative description would be $Ni_{1-x}Cr_xO_{1+y}$. The rock-salt grew in a layer-by-layer mode via an adatom mechanism, consistent with previous reports for various material systems.[8,39-40] Cations diffuse from the bulk to the step-edge growth front of the oxide, Figure 1(b), and react with oxygen at the oxide/gas interface to form a new oxide layer. The propagation of oxide steps terminates when the growth fronts met. The exposed surfaces are {100} which is the lowest energy surface for clean NiO.[41]

For Ni-Cr alloys, Kirkendall voids[29,42-43] were initially observed in the rock-salt film, Figure 2(a), and then as the rock-salt grew the voids moved to the oxide/metal interface, Figure 2(b). It is noted that for similar alloys in previous studies[7-8] there are no reported Kirkendall voids and interfacial voids—it is, however, worth noting there are differences in both the time scale and the experimental geometry compared to the current experiments. The presence of these voids is consistent with other ex situ and in situ TEM experiments where Kirkendall voids have been observed in nanoparticles, wires, and tubes, upon heating or during oxidation.[44-47] When heating a binary system, Kirkendall voids may form as a result of different diffusion rates of atoms.[26-28,48] In the

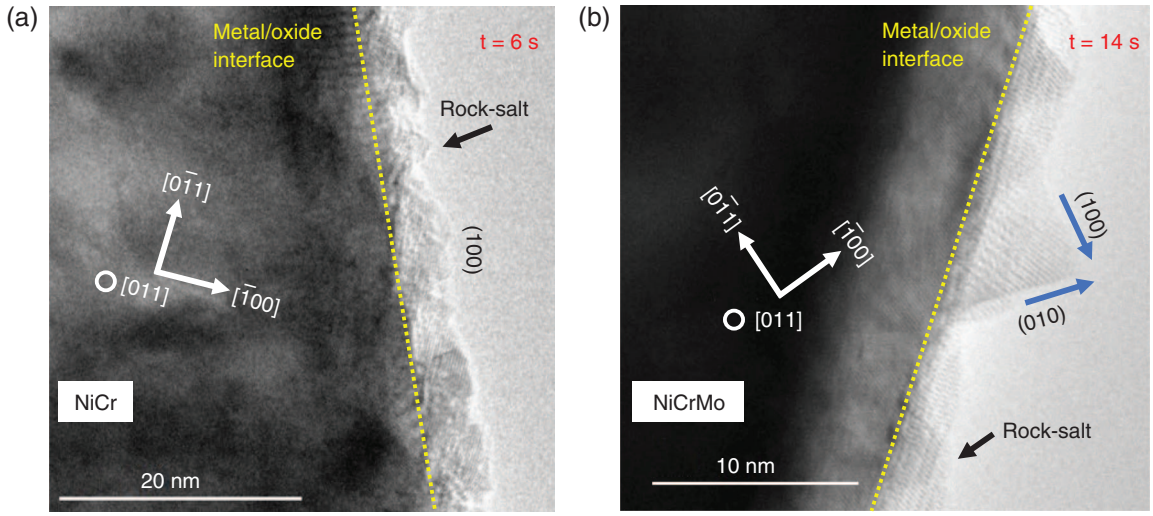

FIGURE 1. *In situ TEM images of initial layer-by-layer growth of NiO on (a) Ni-Cr and (b) Ni-Cr-Mo surfaces. The NiO island has (100) surfaces. The blue arrows in (b) show the layer-by-layer growth direction.*

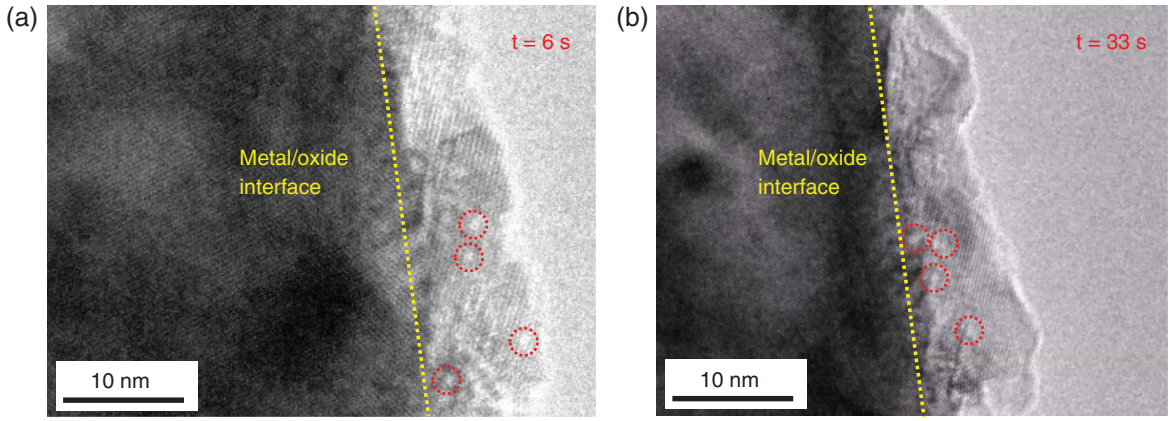

FIGURE 2. *In situ TEM images showing Kirkendall voids (dotted circles) formed (a) in the rock-salt film and (b) near the oxide/metal interface of the Ni-Cr alloy.*

current case, the diffusion rate of cation vacancies is significantly faster than that of oxygen vacancies and the alloy substrate serves as the atomic reservoir to constantly provide cations. The rock-salt oxide forms with a cube-on-cube epitaxy and has a larger lattice parameter than nickel; therefore, the oxide will be compressively strained. Because the external surface can have no tractions, for a nonplanar oxide there will be an inhomogeneous stress gradient within the oxide, more compressive toward the metal/oxide interface. This will drive the voids to condense at the metal/oxide interface and eventually form cavities along the metal/oxide interface, as will be shown later. For the Ni-Cr-Mo alloys, there are no obvious Kirkendall voids in the rock-salt film nor along the metal/oxide interface.

Sequence of Oxides Formation

From the sequential in situ TEM snapshots, in the Ni-Cr alloys a spinel structure similar to the thermodynamic $NiCr_2O_4$ phase was observed to form at the metal/oxide interface shortly (99 s) after the rock-salt initiation and growth, as shown in Figure 3(a). The lattice fringes show the d-spacing is about 2.5 Å (0.25 nm), which is very close to the lattice separation of spinel (311) planes (2.51 Å [0.251 nm]). After the spinel phase formed, further phase formation occurred after about 361 s, Figure 3(b): a phase similar to corundum Cr_2O_3 formed at the metal/oxide interface. The lattice fringes show the d-spacing is about 2.68 Å (0.268 nm), close to the lattice separation of Cr_2O_3 (104) planes (2.66 Å [0.266 nm]).

Prior to the formation of a continuous corundum layer, the rock-salt film continued to grow. During this period, voids in the rock-salt migrated toward the metal/corundum interface forming a cavity, which propagated along this interface and resulted in the corundum detaching from the metal, Figure 3(c). Vacancies might also have been involved in this, but were not detectable.

For Ni-Cr-Mo alloys, the oxidation also started with rock-salt formation. However, after forming a

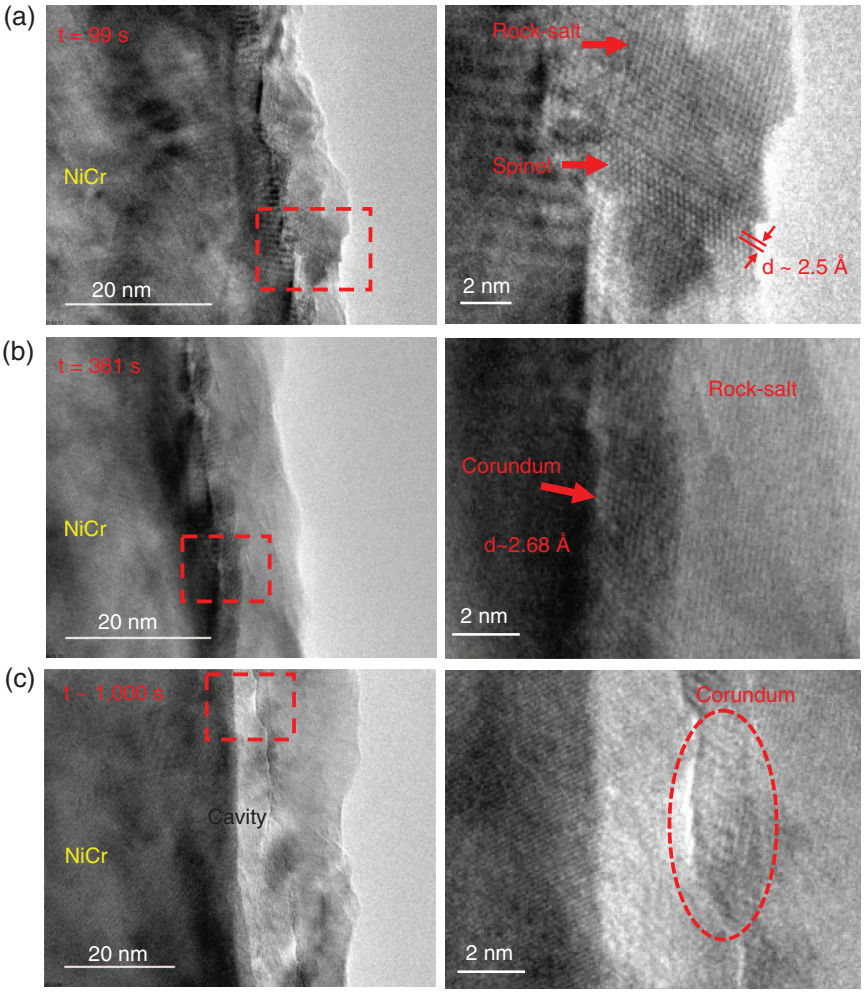

FIGURE 3. *Sequential in situ TEM images of (a) spinel phase similar to $NiCr_2O_4$ initiation, (b) corundum phase initiation, and (c) corundum phase separated from the metal/oxide interface in the Ni-Cr alloy. The enlarged images of the dashed box areas (left) are shown in the right column.*

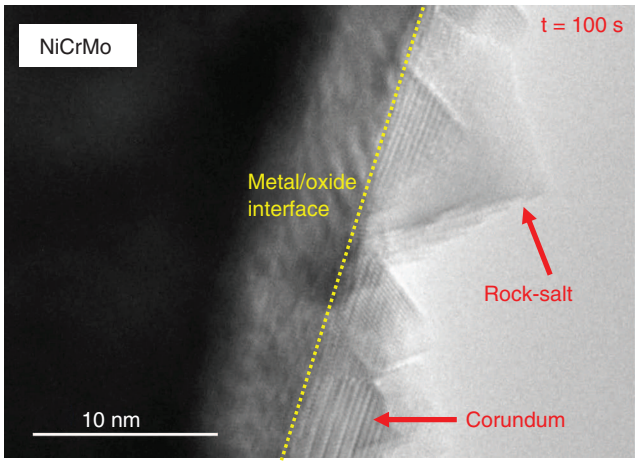

FIGURE 4. *TEM image showing the corundum structure quickly formed after a couple of layers of rock-salt formation.*

couple of layers of rock-salt, Figure 4, the corundum structure is initiated at the metal/oxide interface (~100 s). The lattice fringes show the d-spacing is about 2.49 Å (0.249 nm), which is close to the lattice distance for Cr_2O_3 ($2\bar{1}0$) planes (2.48 Å [0.248 nm]). However, further chemical analysis as described in the next section indicated that the corundum structure had significant Ni doping rather than consisting of pure Cr_2O_3. This is reasonable because Ni_2O_3 is a known metastable phase with the same corundum structure and identical lattice constants to Cr_2O_3.[49-50]

Post-Exposure Chemical Analysis

More detailed chemical analysis on the post-mortem samples after in situ experiments was performed using EELS in the aberration-corrected STEM. From the line-scan profile of Ni-Cr alloys, Figures 5(a) and (b), the outmost $Ni_{1-x}Cr_xO_{1+y}$ layer has about 4 at% ~ 27 at% Cr doping. The reported maximum solubility of Cr in NiO is only 1 at% at 950°C,[51] so clearly the amount of Cr in the rock-salt is much larger than the thermodynamic equilibrium value. This indicates that the kinetic configuration/composition dominates during early-stage oxidation where the solute atoms are captured in the initial oxide.[31]

From the line-scan profile of the Ni-Cr-Mo alloy, Figures 5(c) and (d), two regions are observed, a heavily Cr doped $Ni_{1-x}Cr_xO$ layer over an imperfect $Ni_{2-x}Cr_xO_3$ layer with a Ni:Cr:O composition ratio of about 1:1:3. These results from this corundum structure, discussed above, provide further evidence of solute capture; not only can Cr be captured in rock-salt but Ni can also be captured in corundum. The formation of a metastable $Ni_{2-x}Cr_xO_3$ phase is the consequence of non-equilibrium solute capture.

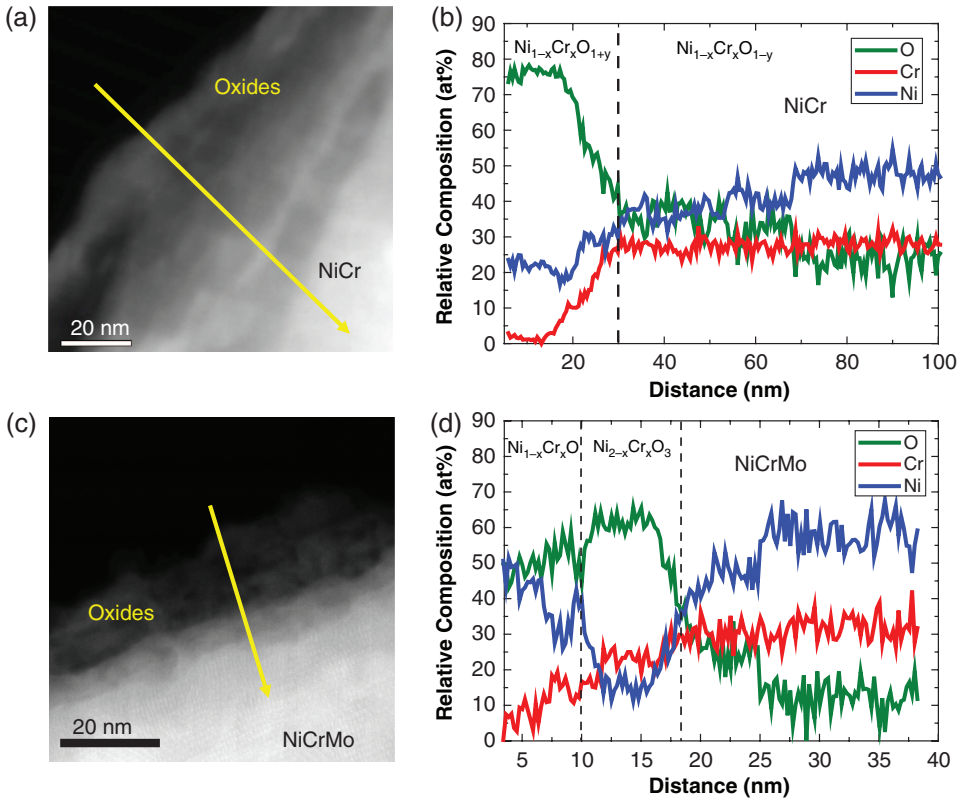

FIGURE 5. *HAADF images of the oxidized samples after in situ experiments for (a) Ni-Cr and (c) Ni-Cr-Mo samples; the yellow arrows indicate the EELS line scanning direction. (b) and (d) are EELS relative composition profiles for Ni-Cr and Ni-Cr-Mo, respectively.*

DISCUSSION

The experimental results demonstrate that during early-stage oxidation thermodynamic equilibrium was not achieved; a large number of atoms such as Ni and Cr were solute trapped. Because of technical limitations in detecting the distribution of this low of a concentration of Mo (~3 at%) in the samples by electron microcopy, atom probe tomography was used and it was confirmed elsewhere that Mo was also captured in the initial oxides formed during the early-stage oxidation/corrosion process.[31]

To briefly clarify why solute atoms are present far beyond conventional solubility limits, the authors have an alloy that is oxidizing with a moving oxidation front that combines point defect migration and physical motion of the interface. The interface therefore has an effective velocity proportional to the rate of incorporation of alloy atoms as cations in the oxide. As the velocity tends to infinity, metal atoms in the alloy cannot achieve equilibrium configurations; they are captured in the oxide with the alloy composition. In the other limit, as the velocity tends to zero, there is a thermodynamic driving force for the alloy atoms to form stable or metastable phases with compositions bounded by solubility limits. With intermediate velocities as in the experiments herein, solute atoms are captured in the oxide with compositions far in excess of the solubility limits. Further details can be found in Yu, et al.[31]

Several points merit further discussion and analysis. The first is the presence of Kirkendall voids which are less probable in the presence of Mo. The second is the preferential formation of solute-captured corundum when Mo is present. It is believed that the two are intimately linked.

As mentioned earlier, Kirkendall voids are linked to differential diffusion, and it is well established that in rock-salt NiO the fastest diffusing species are cation vacancies. If there is too high of a local concentration of vacancies, they can collapse to form voids. As mentioned earlier, the oxide will be compressively strained and for a nonplanar oxide there will be a stress gradient which drives the voids to the metal/oxide interface. Note that this connects to the idea that void formation at the metal/oxide interface may play an important role in protective oxide film breakdown.[52] However, note that the details observed experimentally in the present study are different from this model. For completeness, with a nonplanar system voids might also nucleate in the metal, but the tensile stresses present in the metal near the interface will drive them away from the metal/oxide interface.

The experimental data clearly indicate that there are few Kirkendall voids in the corundum structure. In the rock-salt structure every (octahedral) cation site is occupied, but this is not true in the corundum structure where, assuming the presence of M^{3+}, only 2/3 of the octahedral sites are occupied. This implies that the free energy of vacancies in the sense of the metal-to-oxygen ratio is more favorable if the corundum structure is formed.

Why should Mo promote the formation of the corundum structure? A reasonable hypothesis is that the driver is a change in the vacancy formation energy associated with Mo leading to a smaller number of vacancies, as well as the valence of Mo. From the DFT calculations, if Mo replaces Ni in rock-salt, the expected valence based upon the interatomic distance is 3.29+, determined by a bond-valence sum for a substitutional defect. This indicates that there will be about 2/3 Ni vacancies per Mo. In contrast, if Mo substitutes for Cr in Cr_2O_3 it would have a valence of 4.06+, so there would be about 1/3 Cr vacancies per Mo or nearly half the number of vacancies per Mo cation added. In addition, under oxidizing conditions one would expect a higher valence state for the Mo. These arguments imply that with Mo there will be a change in the free energy of formation of a Mo-doped corundum phase.

To validate the hypothesis, the energy change ΔE_1 was calculated:

$$\Delta E_1 = E(Cr_2O_3) + E(Ni) - E(NiO) - E(Ni(Cr)) - E(O_2) \quad (1)$$

where ΔE_1 is the enthalpy difference between Cr_2O_3 on a Ni substrate and NiO growth on the NiCr alloy substrate. $E(Cr_2O_3)$, E(Ni), E(NiO), and $E(O_2)$ are the total energies of solid Cr_2O_3, Ni, NiO, and O_2 gas molecule, respectively. E(Ni(Cr)) is the total energy of $2\times2\times2$ Ni supercell with one Cr atom substitution. As the benchmark, the lattice constant, band gap, and magnetic moment of Ni or Cr atom in NiO and Cr_2O_3 by meta-GGA (MS2) are shown in Table 1.

The Mo doping effects were calculated by using the equation:

$$\Delta E_2 = E(Cr_2O_3(Mo)) + E(Ni) - E(NiO(Mo)) - E(Ni(Cr)) - E(O_2) \quad (2)$$

where ΔE_2 is the enthalpy difference between Mo-doped Cr_2O_3 growth on the Ni substrate and Mo-doped NiO growth on the NiCr alloy substrate. $E(Cr_2O_3(Mo))$ and E(NiO(Mo)) are the total energies of

TABLE 1

Lattice Constant, Band Gap, and Magnetic Moment of Ni or Cr Atom in NiO and Cr_2O_3 Using the Meta-GGA (MS2)

	NiO		Cr_2O_3	
	This work	Expt.	This work	Expt.
a (Å)	4.15	4.18[53]	4.94	4.95[54]
c (Å)			13.66	13.57[54]
c/a			2.76	2.74[54]
Band gap (eV)	2.11	4.3[55]	2.67	3.4[56]
Magnetic moment (μ_B)	1.56	1.77[57]	2.73	3.8[54]

$2\times2\times2$ Cr_2O_3 and NiO supercell with one Mo atom substitution.

The calculated ΔE_1 and ΔE_2 are –7.70 eV and –7.74 eV per chemical formula with 1/16 Mo doping, which indicates that the thermodynamic driving force of doped rock-salt transforming to doped corundum is increased by $16\times(7.74-7.70) = 0.64$ eV per Mo atom. This is significant and explains the increased nucleation rate of the corundum structure.

CONCLUSIONS

❖ In this work, by using advanced environmental TEM, the structure of oxide and sequence of phase nucleation during the oxidation were provided, and also atomic scale Kirkendall voids formation and migration in the mass transportation process were observed, which is important to understand the morphological stability and breakdown mechanism of protective oxide thin film on alloys surface.

Furthermore, the effects of minor alloying element, such as molybdenum (Mo), were explored on the kinetics of oxide initiation. It was found that Mo doping may stabilize the cation vacancies and inhibit the Kirkendall voids formation by promoting the nucleation of corundum structure. Density functional theory calculations confirm that the thermodynamic driving force of phase transformation from rock-salt to corundum structure is increased by 0.6 eV per Mo atom.

Finally, by combining in situ structural information and ex situ chemical analysis, the non-equilibrium solute capture during the oxidation was found. The solute atoms were captured in the oxides, which exceeded the thermodynamic limits as assumed in many oxidation models. Collectively, these results provide new and deeper insights into the early stages of oxidation and into the effects of alloying, furthering the understanding and improving the design of corrosion resistant alloys.

ACKNOWLEDGMENTS

We acknowledge support from ONR MURI "Understanding Atomic Scale Structure in Four Dimensions to Design and Control Corrosion Resistant Alloys" on Grant No. N00014-16-1-2280. CMA and JCY would like to thank the Petersen Institute for NanoScience and Engineering (PINSE) Nanoscale Fabrication and Characterization Facility (NFCF) and its staff Matt France and Dr. Susheng Tan for their support with the Hitachi H9500 ETEM.

REFERENCES

1. T.M. Pollock, S. Tin, *J. Propul. Power* 22, 2 (2006): p. 361-374.
2. C. Giggins, F. Pettit, *J. Electrochem. Soc.* 118, 11 (1971): p. 1782-1790.
3. H. Hindam, D.P. Whittle, *Oxid. Met.* 18, 5-6 (1982): p. 245-284.
4. P.Y. Hou, J. Stringer, *Oxid. Met.* 34, 3-4 (1990): p. 299-321.
5. B. Kear, F. Pettit, D. Fornwalt, L. Lemaire, *Oxid. Met.* 3, 6 (1971): p. 557-569.
6. D. Douglass, *Corros. Sci.* 8, 9 (1968): p. 665-678.
7. L. Luo, L. Zou, D.K. Schreiber, M.J. Olszta, D.R. Baer, S.M. Bruemmer, G. Zhou, C.M. Wang, *Chem. Commun. (Camb)* 52, 16 (2016): p. 3300-3303.
8. L.L. Luo, L.F. Zou, D.K. Schreiber, D.R. Baer, S.M. Bruemmer, G.W. Zhou, C.M. Wang, *Scrip. Mater.* 114 (2016): p. 129-132.
9. H. Qin, X. Chen, L. Li, P.W. Sutter, G. Zhou, *Proc. Natl. Acad. Sci. USA* 112, 2 (2015): p. E103-109.
10. C.M. Wang, D.K. Schreiber, M.J. Olszta, D.R. Baer, S.M. Bruemmer, *ACS Appl. Mater. Inter.* 7, 31 (2015): p. 17272-17277.
11. C.M. Wang, A. Genc, H. Cheng, L. Pullan, D.R. Baer, S.M. Bruemmer, *Sci. Rep.* 4 (2014): p. 3683.
12. A. Takei, K. Nii, *Trans. Jpn. Inst. Met.* 17, 4 (1976): p. 211-219.
13. D.W. Yun, H.S. Seo, J.H. Jun, J.M. Lee, K.Y. Kim, *Int. J. Hydrogen Energy* 37, 13 (2012): p. 10328-10336.
14. F. Pettit, "Design of Structural Alloys with High-Temperature Corrosion Resistance," in *Fundamental Aspects of Structural Alloy Design*, eds. R.I. Jaffee, B.A. Wilocox (New York, NY: Plenum Press, 1977), p. 597-621.
15. K.R. Peters, D.P. Whittle, J. Stringer, *Corros. Sci.* 16, 11 (1976): p. 791-804.
16. L.Y. Chen, H. Lan, C.B. Huang, B. Yang, L.Z. Du, W.G. Zhang, *Eng. Fail. Anal.* 79 (2017): p. 245-252.
17. M.C. Galetz, B. Rammer, M. Schutze, *Oxid. Met.* 81, 1-2 (2014): p. 151-165.
18. R.S. Lillard, M.P. Jurinski, J.R. Scully, *Corrosion* 50, 4 (1994): p. 251-265.
19. R. Newman, *Corros. Sci.* 25, 5 (1985): p. 331-339.
20. J. Galvele, J. Lumsden, R. Staehle, *J. Electrochem. Soc.* 125, 8 (1978): p. 1204-1208.
21. J.N. Wanklyn, *Corros. Sci.* 21, 3 (1981): p. 211-225.
22. R. Qvarfort, *Corros. Sci.* 40, 2-3 (1998): p. 215-223.
23. C. Lemaitre, A.A. Moneim, R. Djoudjou, B. Baroux, G. Beranger, *Corros. Sci.* 34, 11 (1993): p. 1913-1922.
24. M. Moriya, M.B. Ives, *Corrosion* 40, 2 (1984): p. 62-72.
25. F. Bocher, R. Huang, J.R. Scully, *Corrosion* 66, 5 (2010): p. 055002-01 to 055002-15.
26. E. Kirkendall, L. Thomassen, C. Uethegrove, *Trans. Am. Inst. Min. Metall. Eng.* 133 (1939): p. 186-203.
27. E.O. Kirkendall, *Trans. Am. Inst. Min. Metall. Eng.* 147 (1942): p. 104-109.
28. H. Nakajima, *JOM: J. Min. Met. Mat. Soc.* 49, 6 (1997): p. 15-19.
29. C.A.C. Sequeira, L. Amaral, *Trans. Nonferrous Met. Soc. China* 24, 1 (2014): p. 1-11.
30. L. Klinger, E. Rabkin, *Mater. Lett.* 161 (2015): p. 508-510.
31. X. Yu, A. Gulec, Q. Sherman, K. Lutton, J.R. Scully, J.H. Perepezko, P.W. Voorhees, L.D. Marks, "Non-Equilibrium Solute Capture in Passivating Oxide Films" (2018): https://arxiv.org/abs/1802.07685.
32. G. Kresse, J. Hafner, *Phys. Rev. B* 47, 1 (1993): p. 558-561.
33. G. Kresse, J. Furthmuller, *Phys. Rev. B* 54, 16 (1996): p. 11169-11186.
34. G. Kresse, D. Joubert, *Phys. Rev. B* 59, 3 (1999): p. 1758-1775.
35. P.E. Blochl, *Phys. Rev. B Condens. Matter* 50, 24 (1994): p. 17953-17979.
36. J. Sun, B. Xiao, A. Ruzsinszky, *J. Chem. Phys.* 137 (2012): p. 051101.
37. J. Sun, R. Haunschild, B. Xiao, I.W. Bulik, G.E. Scuseria, J.P. Perdew, *J. Chem. Phys.* 138, 4 (2013): p. 044113.
38. H.J. Monkhorst, J.D. Pack, *Phys. Rev. B* 13, 12 (1976): p. 5188-5192.
39. P.W. Tasker, D.M. Duffy, *Surf. Sci.* 137, 1 (1984): p. 91-102.
40. G. Zhou, L. Luo, L. Li, J. Ciston, E.A. Stach, J.C. Yang, *Phys. Rev. Lett.* 109, 23 (2012): p. 235502.
41. H. Zheng, S.J. Wu, H.P. Sheng, C. Liu, Y. Liu, F. Cao, Z.C. Zhou, X.Z. Zhao, D.S. Zhao, J.B. Wang, *Appl. Phys. Lett.* 104, 14 (2014): p. 141906.
42. L.C.C. Dasilva, R.F. Mehl, *Trans. Am. Inst. Min. Metall. Eng.* 191, 2 (1951): p. 155-173.
43. P.E. Doherty, R.S. Davis, *Ann. N.Y. Acad. Sci.* 101, 3 (1963): p. 787-790.
44. J.G. Railsback, A.C. Johnston-Peck, J. Wang, J.B. Tracy, *ACS Nano* 4, 4 (2010): p. 1913-1920.
45. C.-M. Wang, A. Genc, H. Cheng, L. Pullan, D.R. Baer, S.M. Bruemmer, *Sci. Rep.* 4 (2014): p. 3683.

46. K.N. Tu, U. Gosele, *Appl. Phys. Lett.* 86, 9 (2005): p. 093111.
47. H.J. Fan, M. Knez, R. Scholz, K. Nielsch, E. Pippel, D. Hesse, M. Zacharias, U. Gosele, *Nat. Mater.* 5, 8 (2006): p. 627-631.
48. Q. Yin, F. Gao, Z. Gu, E.A. Stach, G. Zhou, *Nanoscale* 7, 11 (2015): p. 4984-4994.
49. P.S. Aggarwal, A. Goswami, *J. Phys. Chem.* 65, 11 (1961): p. 2105-2105.
50. J.-K. Kang, S.-W. Rhee, *Thin Solid Films* 391, 1 (2001): p. 57-61.
51. C.H. Chen, M.R. Notis, D.B. Williams, *J. Am. Ceram. Soc.* 66, 8 (1983): p. 566-571.
52. L.F. Lin, C.Y. Chao, D.D. Macdonald, *J. Electrochem. Soc.* 128, 6 (1981): p. 1194-1198.
53. S. Sasaki, K. Fujino, Y. Takéuchi, *Proc. Jpn. Acad. Ser. B* 55, 2 (1979): p. 43-48.
54. L.W. Finger, R.M. Hazen, *J. Appl. Phys.* 51, 10 (1980): p. 5362-5367.
55. G.A. Sawatzky, J.W. Allen, *Phys. Rev. Lett.* 53, 24 (1984): p. 2339-2342.
56. J.A. Crawford, R.W. Vest, *J. Appl. Phys.* 35, 8 (1964): p. 2413-2418.
57. A. Cheetham, D. Hope, *Phys. Rev. B* 27, 11 (1983): p. 6964.